Solvent modulation, microstructure evaluation, process optimization, and nanoindentation analysis of micro-Cu@Ag core–shell sintering paste for power electronics packaging

Chen, Haixue ; Wang, Xinyue; Zeng, Zejun ; Zhang, Guoqi; Zhang, Jing ; Liu, Pan

DOI
10.1007/s10854-023-11083-5

Publication date
2023

Document Version
Final published version

Published in
Journal of Materials Science: Materials in Electronics

J Mater Sci: Mater Electron (2023)34:1692

Solvent modulation, microstructure evaluation, process optimization, and nanoindentation analysis of micro-Cu@Ag core–shell sintering paste for power electronics packaging

Haixue Chen[1], Xinyue Wang[1], Zejun Zeng[1], Guoqi Zhang[2], Jing Zhang[3], and Pan Liu[1,4,*]

[1] *Academy for Engineering & Technology, Fudan University, Shanghai 200433, China*
[2] *Department of Microelectronics, Delft University of Technology, 2628 CD Delft, The Netherlands*
[3] *Heraeus Materials Technology Shanghai Ltd., Shanghai 201108, China*
[4] *Research Institute of Fudan University in Ningbo, Ningbo 315336, China*

Received: 19 June 2023
Accepted: 28 July 2023

ABSTRACT

With the development of electronic technology towards high power, miniaturization, and system integration, power electronic packaging is facing increasing challenges, especially for die attachment. This research aims to explore silver-coated copper (Cu@Ag) paste with sufficient mechanical properties and high-temperature reliability, as an alternative solution for silver sintering with lower cost. Firstly, micro-Cu@Ag sintering pastes were investigated under four kinds of polyol-based solvent systems and two types of particle morphologies, which included sphere-type (SCu@Ag) and flake-type (FCu@Ag). Sintering performance and microstructural evolution were compared and analyzed. Notably, sintered joints employing the terpineol–polyethylene glycol solvent system and flake-type morphology displayed a denser microstructure in comparison to SCu@Ag joints. Its bonding strength reached 36.15 MPa, which was approximately 20% higher than SCu@Ag joints. Subsequently, the influence of key sintering process parameters on Cu@Ag joints was analyzed, including sintering temperature, pressure and time. Additionally, high-temperature aging and thermal cycling tests were conducted on the optimized Cu@Ag joints to assess their reliability. Finally, the micromechanical properties of Cu@Ag joints before and after high-temperature aging were further evaluated by nanoindentation including creep properties. The elastoplastic constitutive models of Cu@Ag sintered materials with different particle morphologies were constructed, providing valuable insights for reliability evaluation. The results indicated that FCu@Ag joints exhibited satisfactory creep resistance and high-temperature reliability. In conclusion, the FCu@Ag micro-paste based on the terpineol–

Address correspondence to E-mail: panliu@fudan.edu.cn

https://doi.org/10.1007/s10854-023-11083-5
Published online: 21 August 2023

polyethylene glycol solvent system proposed in this study demonstrated sufficient bonding strength, high reliability, and adequate mechanical properties as an attractive solution for high-temperature power electronics packaging.

1 Introduction

With the rapid development of power electronics applications such as high-speed rail transportation, 5G communication, and electric vehicles, power semiconductor devices are required to work reliably under severe conditions such as high power, high temperature, high frequency, etc. The limitations faced by current silicon-based (Si-based) semiconductor devices in terms of operating temperatures and efficiency have prompted researchers to explore alternatives. Wide-bandgap (WBG) semiconductors, exemplified by silicon carbide (SiC) and gallium nitride (GaN), have emerged as highly promising candidates. In comparison to traditional Si-based semiconductors, these WBG semiconductors present remarkable advantages, including high breakdown voltage, high power density, and high-temperature resistance, etc. [1].

The growing demands for the packaging of WBG power modules present significant challenges for die attach technology [2, 3]. Although conventional lead-free solder alloys such as Sn-based solders and Zn-based solders provide rapid connections to various electronic components, their practical applications are limited due to their low heat resistance and poor corrosion resistance [4, 5]. Hence, numerous investigations have been actively exploring substitution materials and processes [6–8]. Among them, the low-temperature sintered materials represented by sintered silver (Ag) and sintered copper (Cu), have emerged as promising candidates owing to their high melting point, considerable mechanical strength, excellent electrical and thermal conductivity, etc. [9–12]. Compared with sintered Ag, sintered Cu offers a lower material cost and better resistance to electrochemical migration, which has attracted increasing attention in recent years [13, 14]. Nevertheless, the high sintering temperature and high oxidation risk of sintered Cu material led to its limitations for industrial applications. To overcome these shortcomings, the core–shell structure Cu@Ag particles has become an appealing research topic for die attachment [15, 16]. Tian et al. [17] fabricated Cu@Ag nanoparticles through a mild two-step method, which reduced the initial sintering temperature by almost 80 °C compared with sintered Cu, and exhibited excellent performance even after two months of storage. Thomas et al. [18] obtained nanoscale Cu@Ag sintered joints with shear strength above 20 MPa after sintering for 60 min at 200 °C air. Hsiao et al. [19] prepared Cu@Ag particles by low-temperature reduction method and mixed them with submicron Ag particles for sintering. The Cu–Cu bonding strength of 32.7 MPa was achieved at 10 MPa, 275 °C for 30 min, and the resistivity reached 10.4 μΩ cm under the reducing atmosphere. The research in this field has focused more on the sintering properties of Cu@Ag nanoparticles rather than microparticles due to the nano-size effect. However, the high production cost and toxicity risk associated with nanoparticles should not be ignored. So far, few detailed investigations were focused on Cu@Ag micro-scale particles for die attachment.

Furthermore, most previous studies have primarily focused on macroscopic mechanical properties after reliability tests, while micromechanical properties have not been closely examined [20, 21]. Generally, the micromechanical properties of high melting point metals (such as Ag and Cu) were difficult to obtain by the traditional uniaxial tensile method at room temperature, especially the creep properties [22]. Recent years, the nanoindentation test has been proven to be an effective approach to accurately measure micromechanical properties regardless of material structure and volume [23–25]. Hence, it has emerged as an effective approach to accurately measure micromechanical properties, with providing valuable insights into sintered materials. Zhang et al. [26] studied the indentation hardness, plasticity, and initial creep properties of sintered nanosilver joints by nanoindentation tests. They suggested that increasing the sintering pressure from 5 to 30 MPa was beneficial to optimize the indentation hardness, modulus, and creep resistance of the nanosilver sintered joints. Fan et al. [27] characterized the mechanical properties of sintered copper nanoparticles using high-temperature nanoindentation tests and considered that high

auxiliary pressure would lead to a decrease in the temperature sensitivity of hardness and indentation modulus. However, the micromechanical properties of Cu@Ag sintered joints and their evolution under high-temperature aging have not been thoroughly explored. Additionally, there is a lack of research on the elastoplastic constitutive behavior of Cu@Ag sintered materials, which is a crucial aspect for reliability studies.

Therefore, the aim of this research is to explore a suitable Cu@Ag micro-paste for die attachment with sufficient strength and reliability. The influencing factors of obtained joints on sintering properties were discussed, including organic solvent systems, particle morphology, and the sintering process. Besides, the microstructure evolution of Cu@Ag microparticles before and after sintering was observed for sintering mechanism investigation. Comparisons between the influence of key sintering parameters on performances were analyzed to determine the optimal sintering condition for such composite sintering material. Furthermore, the reliability of the Cu@Ag sintered joints after high-temperature aging was examined, as well as high and low-temperature cyclic shock cycles. At last, the micromechanical properties of sintered Cu@Ag joints before and after high-temperature aging were evaluated by using a nanoindentation system, including hardness, elastic modulus, and creep properties. Stress–strain constitutive models of Cu@Ag sintered materials with different particle morphologies were constructed through finite element simulation inversion analysis, providing insights into their elastoplastic behavior. This study contributed to the optimization of sintering pastes by designing organic solvent systems and particle morphology to improve their strength and reliability, which is essential for advanced packaging materials development for high-temperature and high-power module packaging.

2 Experimental

2.1 Materials

Commercial core–shell Cu@Ag microparticles with the size of 1–10 μm were provided by Guangzhou Hongwu Material Technology Co., Ltd. These microparticles were divided into spherical and flake-type shapes, marked as SCu@Ag and FCu@Ag, and the silver coating were 30 wt%. In this experiment, glycerol (G) and triethanolamine (TEA) were purchased from Sinopharm Chemical Reagent, polyethylene glycol (PEG) was from Shanghai Aladdin, and terpineol (T) was provided by Heraeus, Germany. Core–shell Cu@Ag pastes with different organic solvent systems were prepared, and the components of Cu@Ag pastes were shown in Table 1. The prepared pastes were stenciled onto direct-bonded copper (DBC) substrates and pre-dried in a 140 °C nitrogen (N_2) oven for 30 min to remove organics. Before sintering, put the modules with the silver-plated Si dummy (2*2 mm^2) on the hot plate at 175 °C to preheat for 3 min. The sintering process parameters were set at 250 °C, 20 MPa, and 600 s under an N_2 protection atmosphere. The schematic diagram of the sintering process was shown in Fig. 1.

2.2 Characterization analysis

In this experiment, Fourier transform infrared spectroscopy (FT-IR, IRTracer-100, Japan Shimadzu) was performed to characterize the chemical bonding of the organic molecules on the particle surfaces. The thermogravimetric analyzer (SDT-Q600, TA Instruments, USA) was utilized to evaluate the weight change and heat flow behavior of the prepared pastes with different organic solvent systems. The heating rate was 10 °C min^{-1} from room temperature to 400 °C, and the flow rate was 100 ml min^{-1} under N_2 protection atmosphere. The microstructure of Cu@Ag particles was observed by scanning electron microscopy (SEM, Gemini 300) equipped with energy dispersed spectrometry (EDS). In the in-situ heating test,

Table 1 Formulation of Cu@Ag pastes in different organic solvent systems

Pastes	Shape	T	PEG	TEA	G
P1	Flake	+	+	−	−
P2	Flake	+	+	+	−
P3	Flake	+	−	−	+
P4	Flake	+	+	−	+
P5	Spherical	+	+	−	−

Symbols + and − denote contain and exclude in the solvent system

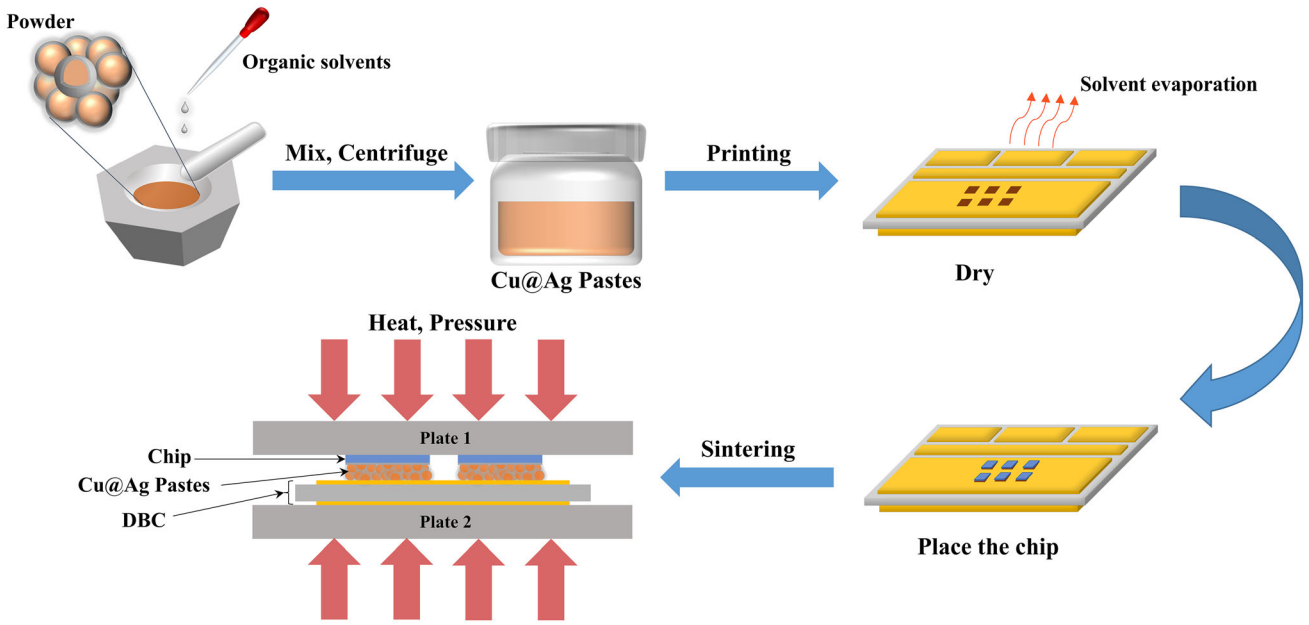

Fig. 1 Schematic diagram of the sintering process

Table 2 Design for nanoindentation experiment of Cu@Ag samples

Experiment conditions	Loading rate (mN s^{-1})	Maximum load (mN)	Holding time (s)
Group 1	0.4	20	30
Group 2	0.8	20	30
Group 3	1.2	20	30
Group 4	0.8	10	30
Group 5	0.8	30	30
Group 6	0.8	20	300

the heating rate was 10 °C min^{-1} from room temperature to 450 °C. The high-temperature aging test was conducted in a blast oven (DHG-9035 A) set at 250 °C for 400 h, taken out samples after the settled time (0 h, 50 h, 100 h, 150 h, 200 h, 300 h, 400 h). The high and low-temperature cycle test was conducted in the cold and heat shock chamber ($VT^3$7006S2) from − 55 to 150 °C. The cycle conditions were 2 cycles h^{-1} for 450 cycles, and a set of samples were taken out after each interval of 50 cycles. The shear strength of the sintered joints was measured by a push–pull tester (Dage-4000), with a shear speed of 0.3 mm s^{-1} and a shear height of 50 μm.

Nanoindentation tests were conducted on the Bruker Hysitron TI980 nanoindentation instrument using a standard Berkovich indenter, with the indenter material was diamond. The SCu@Ag and FCu@Ag samples were tested after different high-temperature aging time (0 h, 50 h, 100 h, 200 h, 400 h). The specific experimental test conditions were detailed in Table 2. To minimize the influence of sample surface roughness, the test samples were finely polished before the experiment, and the distance between adjacent indentations was more than three times the size of the indentations. More than 5 test points were recorded under each experimental condition, and the obtained data were averaged. Equivalent indentation stress (σ) was defined as the ratio of impingement load to indentation projection area, expressed as follows:

$$\sigma = \frac{P}{A}, \tag{1}$$

where P is the load and A is the indentation projection area.

For an ideal Berkovich head, the projected area A and the contact depth h_c were calculated using the following formula:

$$A = 24.56{h_c}^2, \tag{2}$$

$$h_c = h_{max} - \epsilon\frac{P_{max}}{S} = h_{max} - \epsilon(h_{max} - h_r), \tag{3}$$

where h_{max} is the maximum pressing depth of the indenter, S is the contact stiffness, $\epsilon$is the shape correction factor of the indenter (ϵ = 0.75), and h_r is the remaining depth after unloading.

Based on the Oliver–Pharr model [28], hardness (H) and elasticity modulus (E) were expressed as:

$$H = \sigma = \frac{P_{max}}{A}, \tag{4}$$

$$E_r = \frac{\sqrt{\pi}}{2\beta} \times \frac{S}{\sqrt{A}}, \tag{5}$$

$$\frac{1}{E_r} = \frac{1 - v_i^2}{E_i} + \frac{1 - v^2}{E}, \tag{6}$$

where E_r is the reduced modulus and a constant related to the shape of the indenter (β = 1.034). E_i and v_i are the elastic modulus and Poisson's ratio of the indenter material ($E_i = 1140$ GPa, $v_i = 0.07$), while E and v are the elastic modulus and Poisson's ratio of the test material, respectively.

Contact stiffness (S) is defined as the slope at the initial stage of the unloading curve in the load-indentation depth curve, which was expressed as:

$$S = \frac{dP}{dh}. \tag{7}$$

In the nanoindentation experiment, when the load is maintained for a while, the metal material will undergo creep deformation, resulting in creep displacement. The creep rate ($\dot{h}$) and creep strain rate ($\dot{\epsilon}$) of the samples were calculated by the following formula:

$$\dot{h} = \frac{dh}{dt}, \tag{8}$$

$$\dot{\epsilon} = \frac{\dot{h}}{h} = \frac{1}{h}\frac{dh}{dt}. \tag{9}$$

On the other hand, the hardness of samples at room temperature can also be expressed as:

$$H = C(\dot{\epsilon})^m, \tag{10}$$

wherein, C is the proportionality constant related to the material structure, and m is the strain rate sensitivity index.

Thus, combined with formulas (4), (9), and (10), the strain rate sensitivity index m was described as:

$$m = \frac{\partial ln H}{\partial ln \dot{\epsilon}} = \frac{\partial ln(P/A)}{\partial ln(\dot{h}/h)}. \tag{11}$$

2.3 Finite element simulation inversion analysis

Typical nanoindentation load–displacement curve (P–h curve) of the metal elastic–plastic materials were shown in Fig. 2a. The loading curve in the P–h curve satisfied Kick's law [29], as depicted in the Eq. (12):

$$P = Ch^2. \tag{12}$$

In addition, the total work (W_t) in the loading phase can be expressed as the sum of elastic work (W_e) and plastic work (W_p), as demonstrated in Eq. (13):

$$W_t = W_e + W_p. \tag{13}$$

The power-law strengthening model was commonly used to describe the stress–strain relationship of metal materials, as shown in Fig. 2b, which was expressed as follows [30]:

$$\sigma = \begin{cases} E\epsilon(\sigma \le \sigma_y) \\ R\epsilon^n = \sigma_y\left(1 + \frac{E}{\sigma_y}\epsilon_p\right)(\sigma > \sigma_y) \end{cases}, \tag{14}$$

where E is Young's modulus, R is the strength coefficient, n is the strain strengthening index, σ_y is the yield strength, and ε_p is the strain at the plastic stage.

In this study, an axisymmetric two-dimensional ANSYS finite element model (FEM) was constructed to simulate the indentation response of Cu@Ag samples, as depicted in Fig. 3a. Since the FEM required a unified unit system, the unit of length is μm, the unit of time is s, the unit of elastic modulus and stress is MPa, and the unit of force is mN. To adhere to Saint-Venant's principle and achieve better grid accuracy, the FEM model was divided into four parts. In this experiment, the maximum displacement of 1000 nm was obtained by the continuous stiffness measurement (CSM) technique with a loading strain rate of 0.05 s^{-1}. The elastic–plastic constitutive model of Cu@Ag sintered particles was established through inversion calculation, and the inversion analysis flow chart was shown in Fig. 3b.

3 Results and discussion

3.1 Effect of solvent modulation on sintering properties

The sintering performance was significantly impacted by the organic solvent system used as the carrier

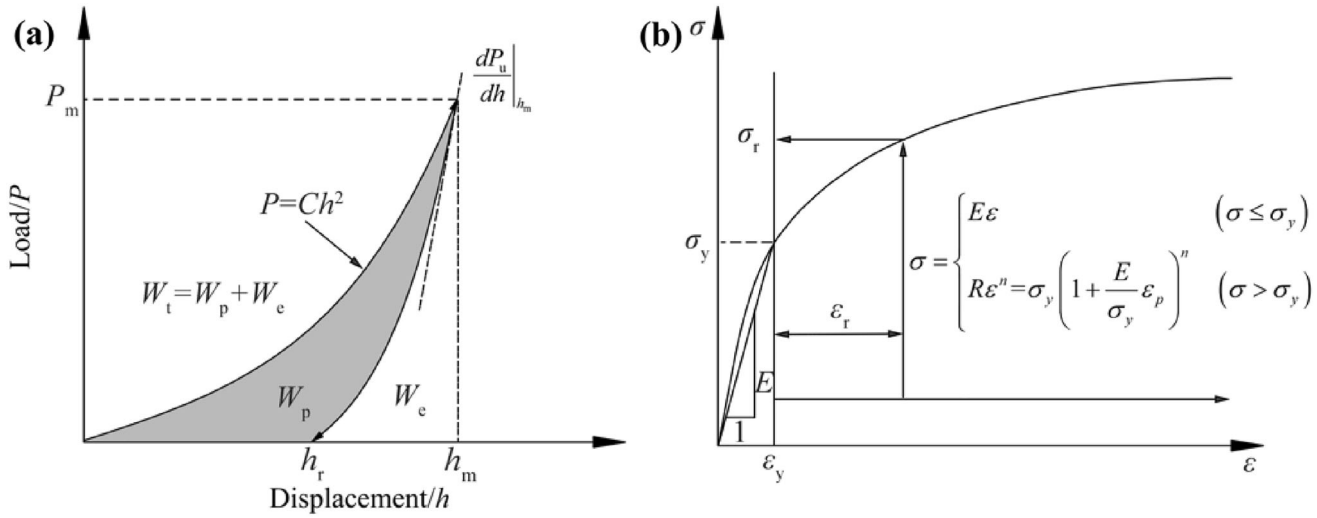

Fig. 2 **a** Typical load–displacement curve of nanoindentation, **b** power-law constitutive model curve of material elastic–plastic behavior

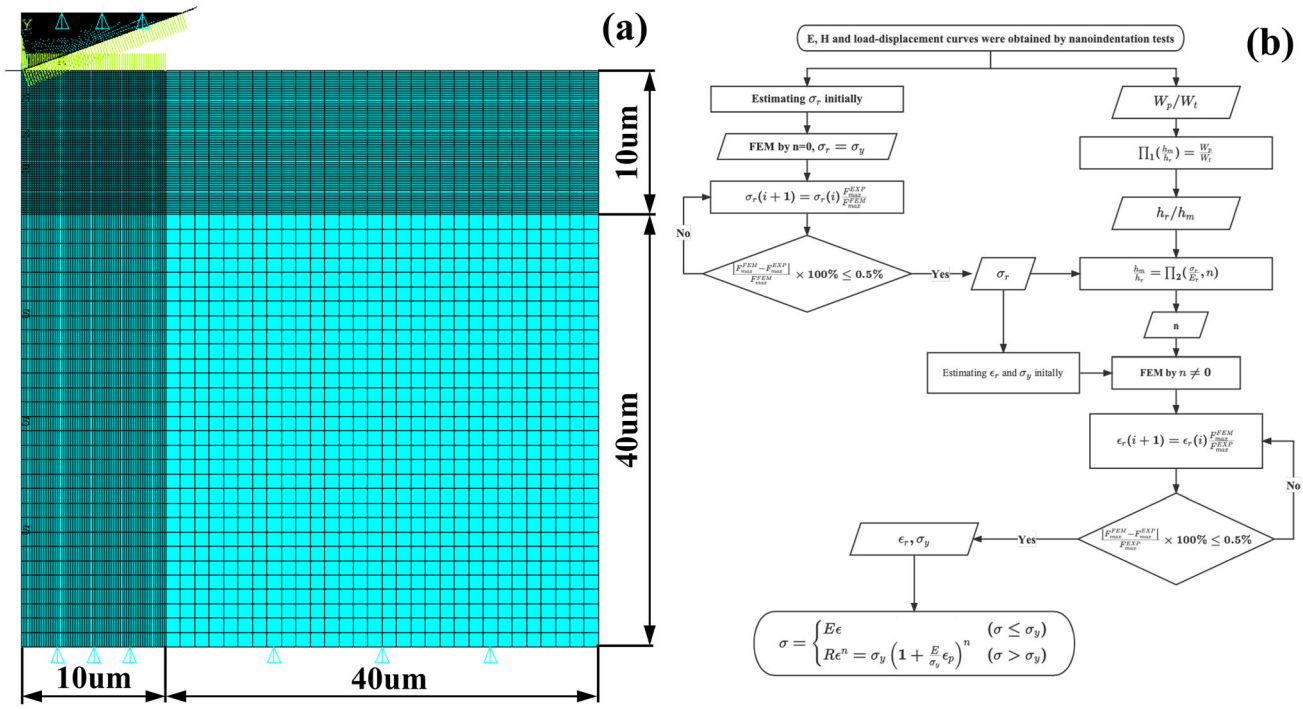

Fig. 3 **a** Finite element geometric model of nanoindentation, **b** flow chart of inversion analysis

for the sintering pastes. Therefore, the internal characteristics of the solvent systems were investigated first, with a focus on FTIR analysis and thermogravimetric analysis. FTIR analysis offered valuable insights into the chemical properties of the sintering pastes, encompassing chemical bonds, functional groups, and molecular structure. Besides, it facilitated the detection of potential impurities that could adversely affect the performance and reliability of Cu@Ag pastes. Figure 4a represented the FTIR spectra of Cu@Ag pastes with different organic solvent systems. It showed that the obvious absorption peak at 3463 cm^{-1} to 3309 cm^{-1}, which was related to the stretching vibration of the hydroxyl group (–OH). By contrast, P3 paste produced a relatively strong absorption peak due to its solvent system containing more glycerol and terpineol. The absorption peaks near 2869 cm^{-1} and 1455 cm^{-1} represented the

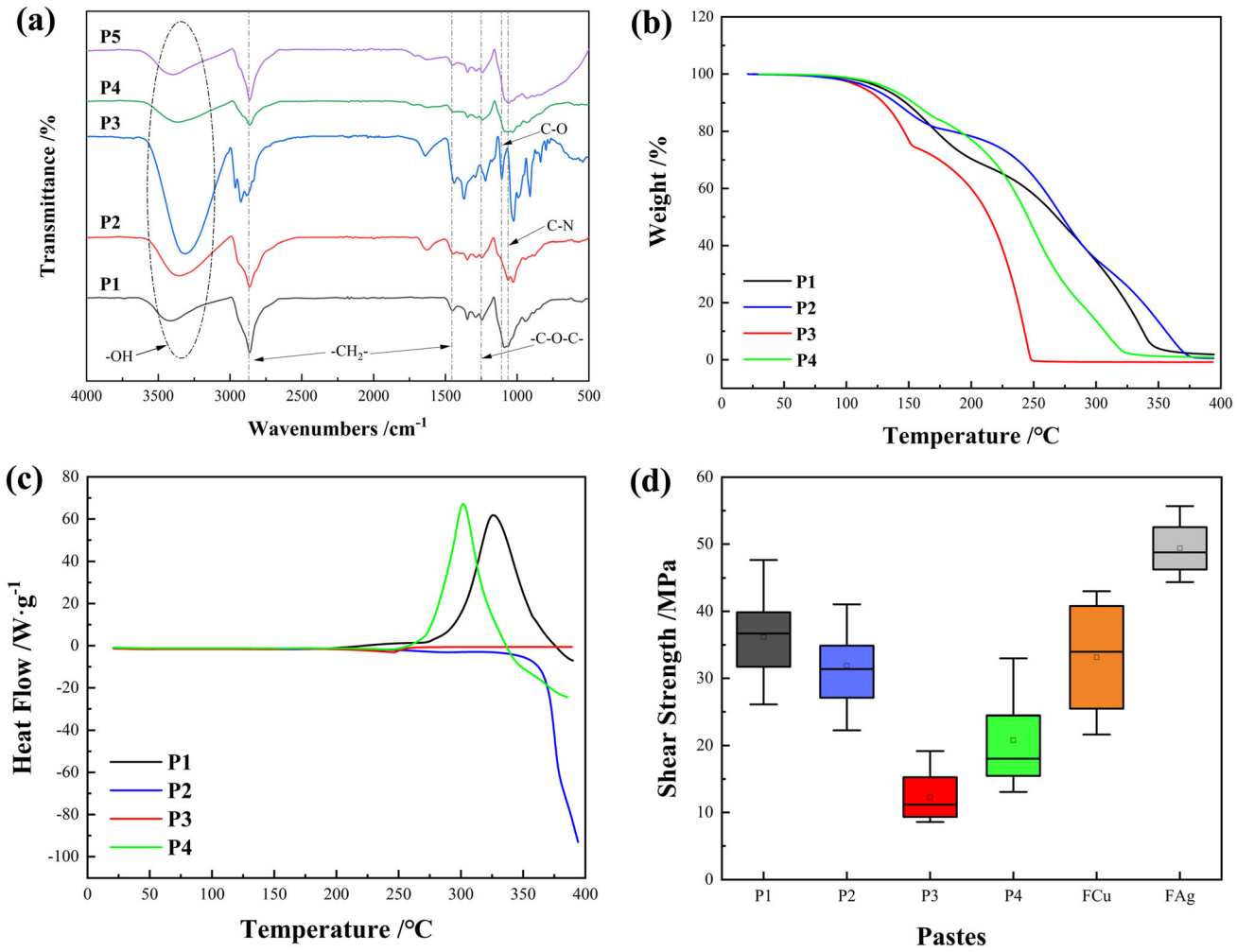

Fig. 4 **a** FTIR spectrum of P1–P5 pastes, **b** TG and **c** DSC curves of P1–P4 pastes, **d** shear strength of sintered joints

stretching and bending vibrations of methylene (–CH2–), respectively. Only the P3 paste did not exhibit an ether bond (C–O–C) absorption peak at 1250 cm^{-1}, this is because only P3 had no polyethylene glycol. Similarly, the C–N bond exhibited stretching vibration around 1063 cm^{-1} to confirm that P2 contained triethanolamine. There were no additional metal oxide absorption peaks were observed below the 700 cm^{-1} regions, indicating that P1–P5 pastes all had high-quality purity and oxidation resistance.

Thermogravimetric analysis was employed to investigate the thermal behavior of sintering pastes, offering valuable insights for optimizing paste composition and sintering parameters. Thus, the differences between the thermal behaviors of the P1–P4 sample solvent systems were discussed, as displayed in Fig. 4b, c. The results indicated that the P3 sample underwent rapid decomposition before 250 °C, resulting in a considerable number of pores in the sintered layer, which adversely affected the bonding strength and reliability. Almost all of the organic components in the pastes were volatilized and decomposed at temperatures below 350 °C, leaving less than 4% organic residue, except for the P2 sample. The P1 sample showed an exothermic peak at 326.3 °C with a weight loss of 44.64%, attributed to the decomposition of the PEG component. Similarly, the P4 sample showed an exothermic peak at 301.8 °C with a weight loss of approximately 35.08%, which was ascribed to the decomposition of propanetriol to neutralize some of the heat. Furthermore, the shear strength of joints sintered by P1–P4 pastes with different solvent systems was investigated, as shown in Fig. 4d. Among these four organic solvent systems, the shear strength of P1 joints was the highest while

P3 was the lowest, with an average value of 36.15 MPa and 12.28 MPa, respectively. The results verified the above thermogravimetric analysis. The shear strength of the P2 joints was slightly lower than P1, as the P2 paste was found chemically unstable during the storing procedure. The P4 joints had higher average bonding strength than the P3 joints since the spatial barrier effect of the dispersant PEG avoided agglomeration between the Cu@Ag particles. Additionally, the shear strengths of pure copper and pure silver sintered particles in the P1 organic solvent system were tested for comparison. The shear strength of sintered Cu joints was slightly lower than that of Cu@Ag sintered particles at 33.13 MPa, and the joint bonding quality level fluctuated greatly. On the other hand, the shear strength of sintered silver joints achieved 49.39 MPa, while its industrial application was limited by the high cost. As a result, the P1 paste based on FCu@Ag microparticles exhibited great potential for die attachment due to its good chemical stability, sufficient shear strength, and potential low cost.

3.2 Effect of sintered particle microstructure on sintering properties

The sintering process was significantly influenced by particle morphology due to its relation to surface energy, thus it is essential to investigate its influence on the sintering performance. The microstructure of the initial Cu@Ag core–shell particles before sintering was illustrated in Fig. 5a–d. The particle size of SCu@Ag was observed to be relatively uniform at about 1–2 μm, while FCu@Ag was relatively large at around 10 μm. Both types showed a great coating effect that effectively insulates the copper core from oxygen. Figure 5e showed that there was no significant change occurred between the FCu@Ag particles during the in-situ heating process, inferring that the solvent system in the sintering paste played an important role in connecting the metal particles and initiating the sintering process. Figure 6 showed the morphology of the sintered joints, which revealed that the sintered Cu@Ag layer had a dense sandwich structure. Compared with SCu@Ag particles, FCu@Ag particle sizes were larger, which should lead to larger porosity of sintered layer with the same silver content. Despite this, the sintered FCu@Ag joints still exhibited a dense structure and made close contact with the substrate surface after sintering. Based on the observations, the contact between SCu@Ag particles was point contact, while that of FCu@Ag particles was surface contact. On the other hand, the relatively larger surface area of FCu@Ag particles also increased the probability of contact. Thereby, flake-type Cu@Ag particles were more inclined to form denser connections during diffusion sintering. From Fig. 6c, f, it was concluded that the Ag shell in FCu@Ag particles exhibited relatively better protective and antioxidant effects during the sintering process.

It is of great importance to analyze the necking growth among Cu@Ag particles during the sintering. Figure 7 displayed the microscopic morphology of Cu@Ag sintered particles, and the necking growth between Cu@Ag particles was clearly observed. During the sintering process, the organic matter gradually decomposed and volatilized, leading to the sintering of contact areas between the Cu@Ag particles. On one hand, the Ag shell on the surface of Cu@Ag particles entered the tiny gaps between the particles through sintering. With further sintering, the porosity of the sintered joints decreased gradually. On the other hand, with the partial disappearance of the Ag layer at the interface of Cu@Ag sintered particles, copper cores contacted and diffused with each other, resulting in the formation and coarsening of Cu sinter necks. In summary, the results showed that the FCu@Ag sintered particles exhibited condensed sintered structures which linked with high reliability under high-temperature and high-power conditions.

3.3 Effect of process optimization and reliability test on sintering performance

To investigate the influence of sintering process parameters on mechanical properties, the shear strength results and full factor analysis of P1 sintered joints under different process parameters were shown in Fig. 8. The results indicated that the shear strength of joints sintered at 200 °C was below 10 MPa, suggesting the absence of effective sintering. As the sintering temperature rose from 200 to 250 °C, the bonding strength of Cu@Ag joints was improved. When the temperature rose to 250 °C, the shear strength sintered at 20 MPa for 5 min reached 22 MPa, which was 83.3% higher than that at 225 °C under the same sintering condition. Furthermore, the

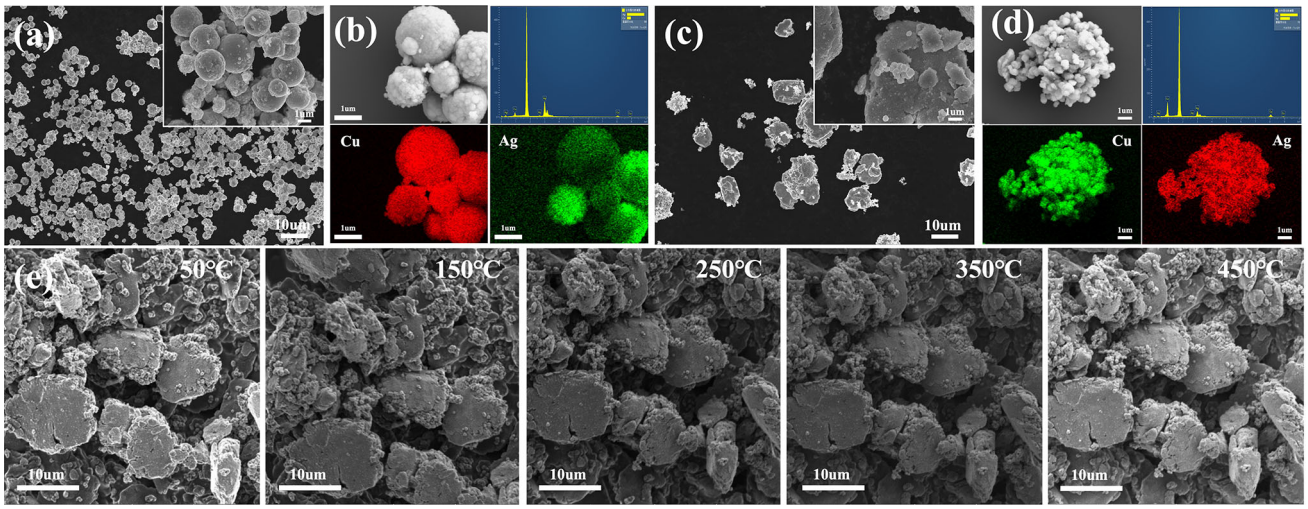

Fig. 5 SEM and EDS mapping images of initial SCu@Ag (**a**, **b**) and FCu@Ag (**c**, **d**) particles; **e** In-situ SEM image of FCu@Ag particles

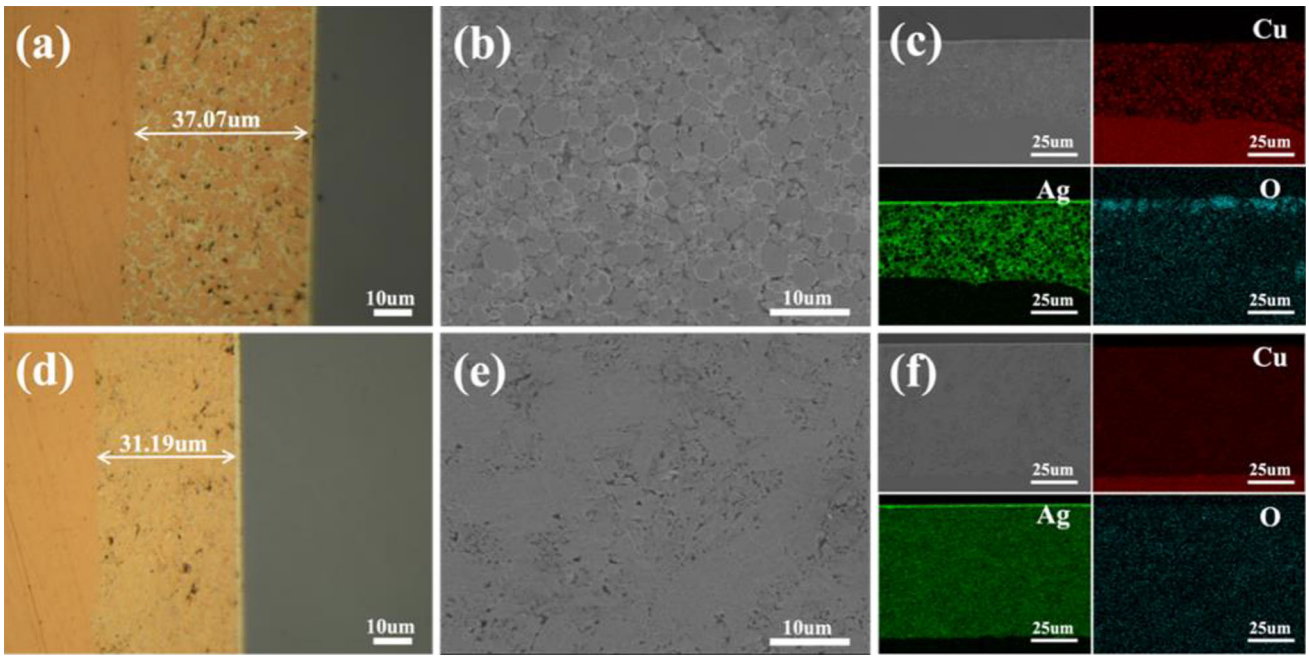

Fig. 6 **a**–**c** SCu@Ag and **d**–**f** FCu@Ag samples after sintering: **a**, **d** cross section of the joints, **b**, **e** SEM images and **c**, **f** EDS mapping

shear strength of the joints sintered for 10 min reached 36.15 MPa, which was sufficient for die-attach applications. From Fig. 8b, it was clearly seen that both sintering temperature, time and pressure effectively improved the shear strength of FCu@Ag sintered joints. Regarding P1 paste, the sintering temperature was identified as the most critical factor, while the sintering pressure had the least impact. Considering that not only the sintering performance and efficiency should be guaranteed, but also the chip and substrate need to be protected from cracking, the optimal sintering process parameters were recommended as 250 °C, 20 MPa, 10 min.

To simulate the harsh and complex temperature environment faced by high-power devices, high-temperature aging tests and thermal cycling tests were conducted on the sintered joints, as depicted in Fig. 9. Before aging, the initial shear strength of the FCu@Ag joints exceeded that of SCu@Ag joints, which was consistent with the microstructure

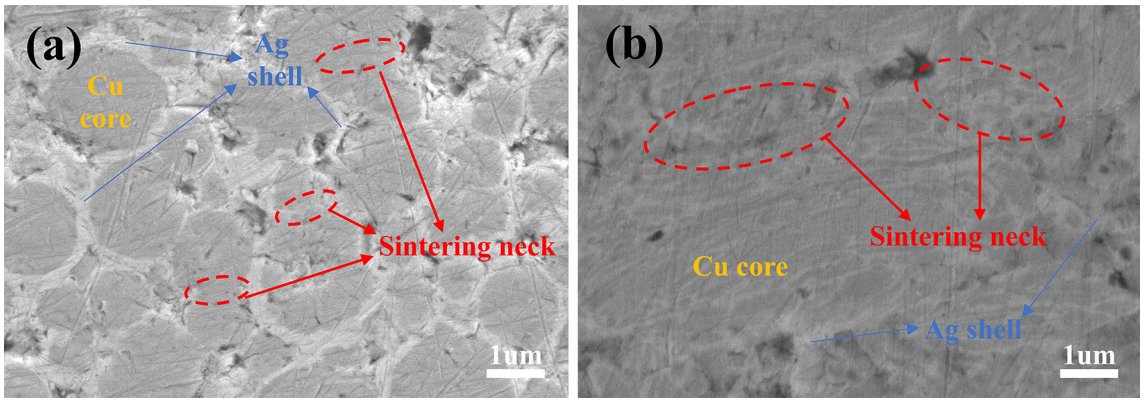

Fig. 7 Cross-sectional SEM images of Cu@Ag sintered microparticles: **a** SCu@Ag, **b** FCu@Ag

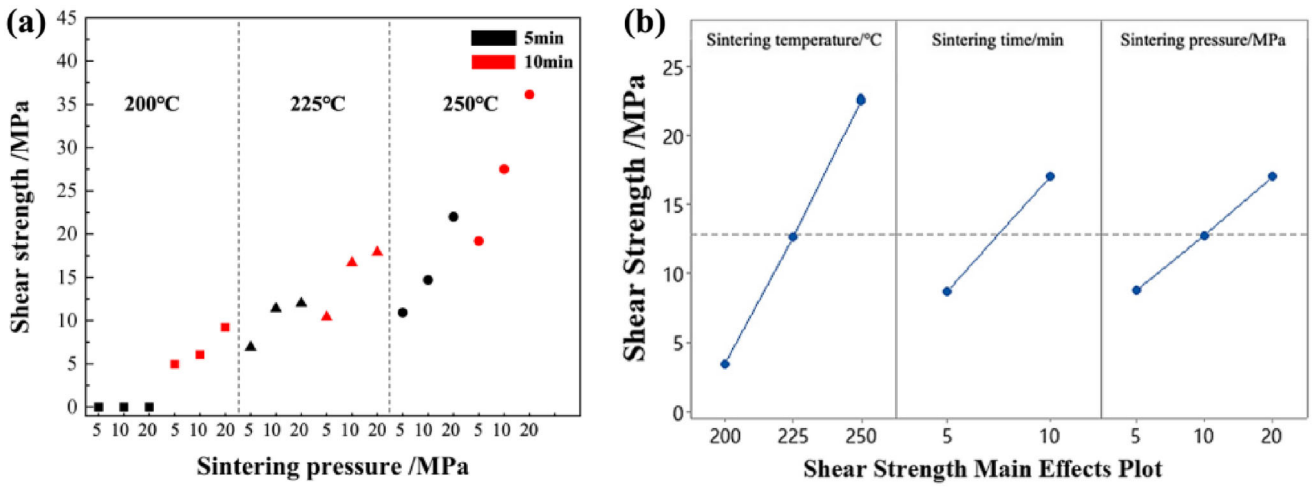

Fig. 8 Shear strength of sintered FCu@Ag joints: **a** under different sintering process conditions, **b** main effect diagram

analysis in Sect. 3.2. After the high-temperature aging test, the average bonding strength of SCu@Ag joints rose to 52.53 MPa after 50 h aging, which was an increase of 73% from the initial. Similarly, the mean strength of FCu@Ag joints also increased to 63.49 MPa after 50 h aging, which was 76% higher than before. In the initial 100 h of high-temperature aging, the shear strength of both SCu@Ag and FCu@Ag samples showed the fastest increase. The results indicated that the shear strength of SCu@Ag and FCu@Ag joints both improved after 400 h of high temperature aging at 250 °C, demonstrating their stable working properties under high operating temperatures, particularly for FCu@Ag joints. On the other hand, the thermal cycling test performed from − 55 to 150 °C and 2 cycles h^{-1} conditions showed the decreasing of shear strengths. After only 50 cycles in the thermal cycling test, the shear strength of SCu@Ag joints rapidly declined from the initial value of 30.31–19.28 MPa by 36.4%. The bonding strength of FCu@Ag joints decreased slower than SCu@Ag joints.

Additionally, the microstructural evolution of Cu@Ag samples during high-temperature aging was observed, and the cross-sectional SEM images were recorded in Figs. 10 and 11. Both the SCu@Ag and FCu@Ag samples demonstrated a trend of decreasing porosity with increasing high-temperature aging time. The rapid densification after 100 h, as shown in Fig. 10, corresponded to the rapid shear strength increase shown in Fig. 9a. The increased bonding strength after high-temperature aging was not only attributed to the further decomposition and dissipation of chemical residues but also the densification of the sintered structure.

Moreover, it also benefited from the tighter metal bonding formed by the diffusion between Cu and Ag at the interface of Cu@Ag particles after aging, as

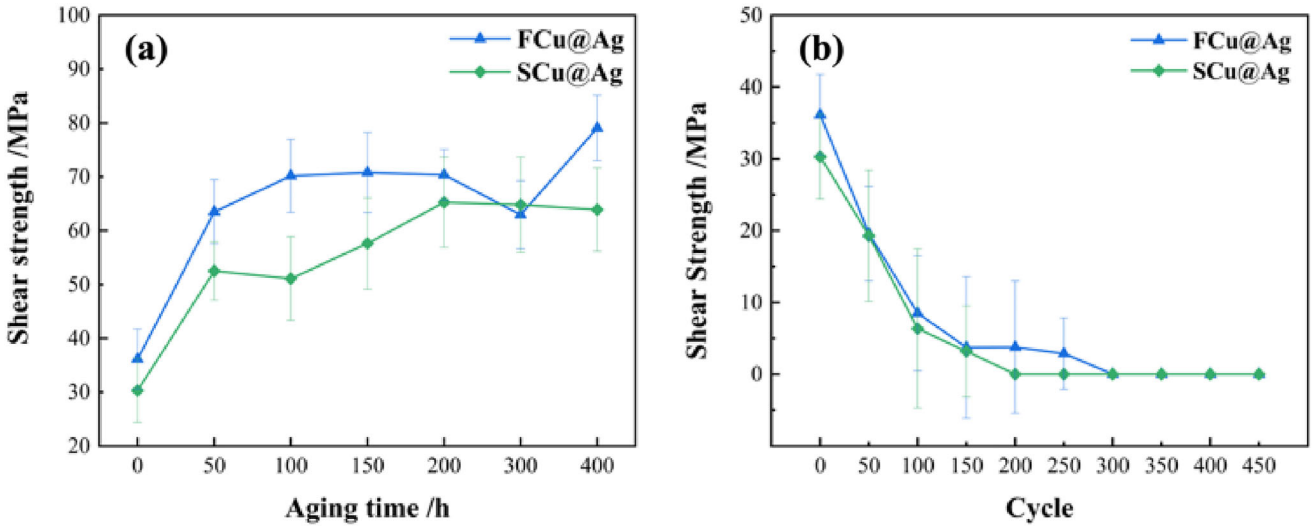

Fig. 9 Shear strength of sintered joints: **a** high-temperature aging, **b** thermal cycle impact

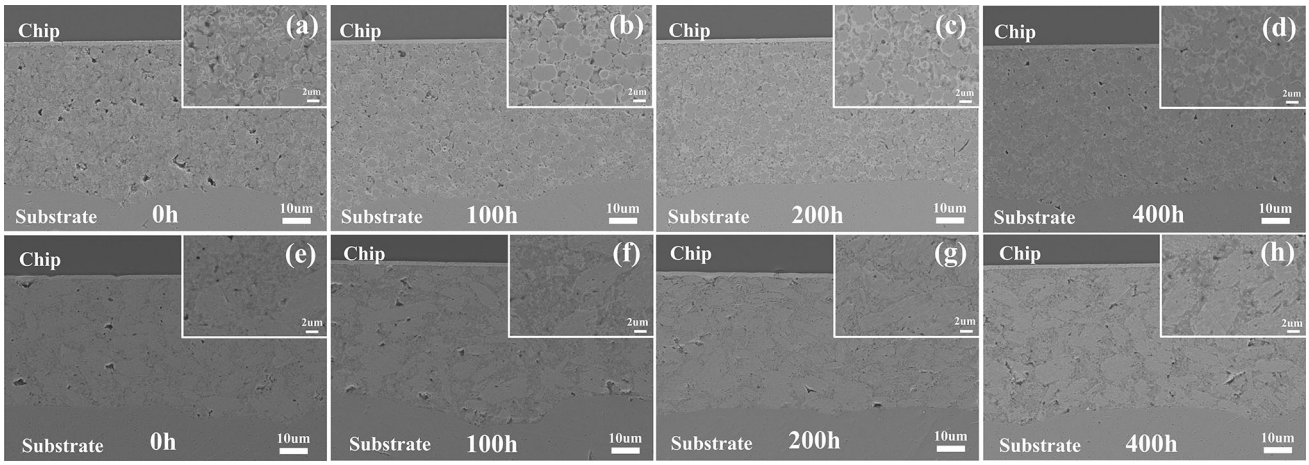

Fig. 10 SEM images of cross section of Cu@Ag samples after different high temperature aging time: **a**–**d** SCu@Ag: 0 h,100 h, 200 h, 400 h; **e**–**h** FCu@Ag: 0 h, 100 h, 200 h, 400 h

shown in Figs. 11 and 12; Table 3. The sintering behavior indicated that the copper cores tended to diffuse and gathered into the contact interface or structural void between particles, after the dewetting of the Ag layer. Since Cu and Ag shared the same face-centered cubic crystal structure, high-temperature aging also promoted their interdiffusion, thereby improved the bonding quality. Besides the microstructure capture through SEM, EDS is also applied for sintering mechanism analysis. The increase in oxygen content was observed from the EDS mapping results, probably due to the formation of copper oxide aggravated by aging tests. The separated Ag shell was filled into the tiny pores left by the volatilization of organic matter. Although the copper oxide structure formed was relatively loose, the densification of the sintered structure had a relatively dominant impact on the performance of the Cu@Ag joints, resulting in enhanced shear strength. It was worth mentioning that there were also differences in the shapes of pores formed by SCu@Ag and FCu@Ag sintered particles, which were spherical pores and narrow strip pores, respectively. Combined with the strength results, it was inferred that compared with spherical pores, the narrow and long pores in the non-shear failure direction may have a stronger hindering effect on crack propagation. Figure 13 illustrated the sintering evolution process of Cu@Ag particles. In contrast to the isotropic sintering of spherical particles, flake-type Cu@Ag particles

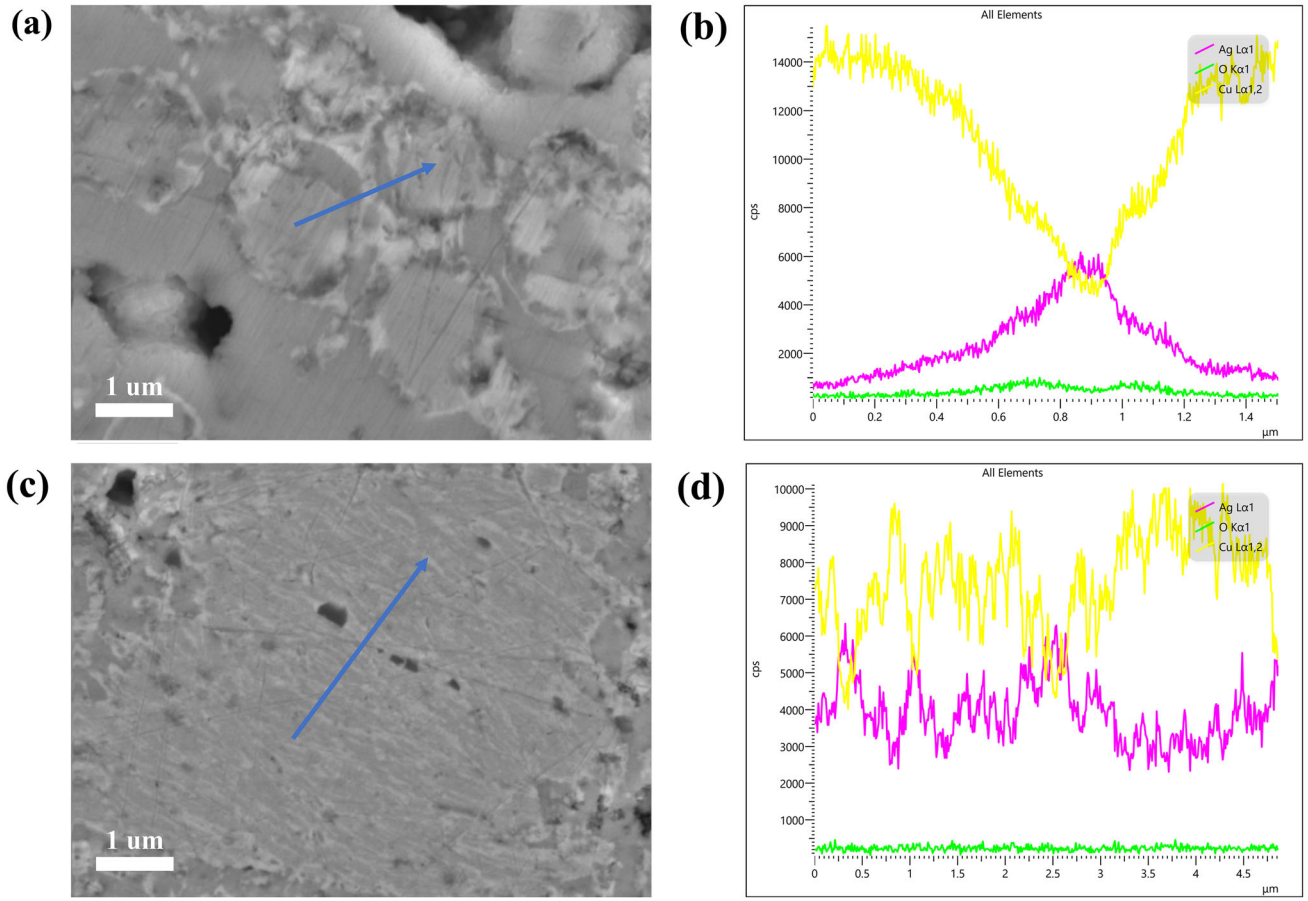

Fig. 11 SEM images and EDS mapping of sintered joints after 400 h aging: **a**, **b** SCu@Ag, **c**, **d** FCu@Ag

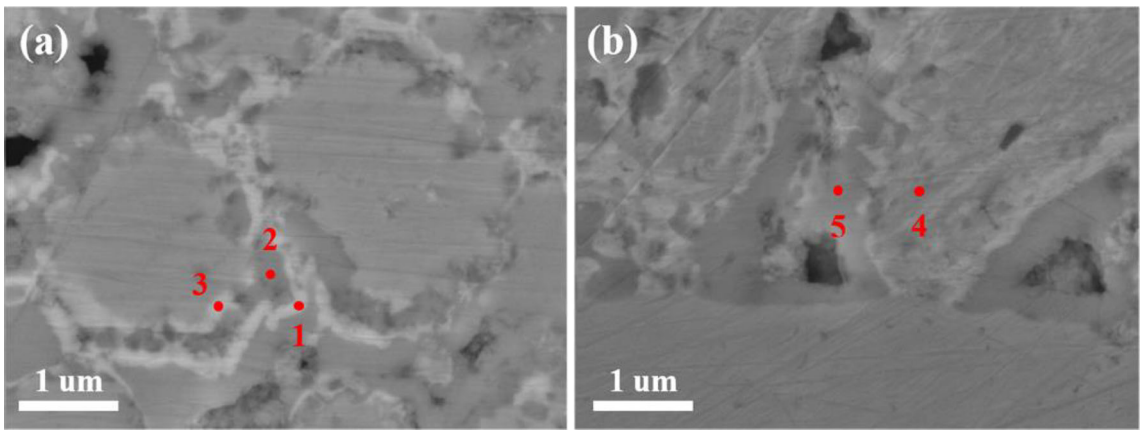

Fig. 12 SEM image of Cu@Ag sintered particle after 400 h aging: **a** SCu@Ag, **b** FCu@Ag

exhibited anisotropic sintering, which was more conducive to accelerating the sintering process of Cu@Ag particles. Moreover, the bridging effect between the flake-type particles also enhanced the internal connection of the sintered joints, leading to improved mechanical properties. In conclusion, FCu@Ag joints embraced better resistance to high temperature and thermal cycling, indicating their excellent reliability to satisfy strict operating temperature requirements of power devices.

3.4 Nanoindentation analysis of sintering properties

3.4.1 *Main influencing factors of room temperature nanoindentation test*

Nanoindentation technology has been demonstrated to be an effective method for accurately evaluating the micromechanical properties and fatigue behavior of sintered materials for chip interconnection, thereby contributing to the improvement of chip reliability and performance. At first, it was necessary to investigate the effects of nanoindentation parameters on the load–displacement curves and micromechanical properties of Cu@Ag joints, were shown in Fig. 14. The Cu@Ag samples under the indenter underwent elastoplastic deformation during the loading process, while the elastic recovery occurred during the unloading process. Under the same load condition, the higher the loading rate, resulting in a smaller indentation depth and steeper load–displacement curve. Similarly, at a fixed loading rate, the indentation depth was positively correlated with the applied load. This correlation can be attributed to the release of stored elastic deformation energy during the load-holding stage, which results in greater indentation depth. Obviously, under the same test conditions, the maximum indentation depths of SCu@Ag samples were greater than FCu@Ag samples, indicating that the latter exhibited stronger impact resistance. The hardness of Cu@Ag samples decreased with the increase in load, indicating that there was a slight indentation size effect. In contrast, indentation performance was more sensitive to load variation rather than loading rate. After comprehensive consideration, conditions of 0.8 mN s^{-1} and 20 mN were selected for subsequent nanoindentation experiments.

Table 3 EDS data for different positions in Cu@Ag sintered particles

Elements (wt%)	Point 1	Point 2	Point 3	Point 4	Point 5
Cu	37.08	52.12	45.15	56.46	77.62
Ag	57.50	40.89	52.16	42.08	15.33
O	5.42	7.00	2.69	1.46	7.04

3.4.2 *Hardness and elasticity modulus*

Nanoindentation technology offers powerful advantages of high resolution and high sensitivity in the nanometer scale, providing more accurate information on the micromechanical properties of sintered materials, such as hardness and elastic modulus, and helping to understand their deformation and failure under stress. Figure 15 presented the average hardness and elastic modulus values of Cu@Ag joints after different high-temperature aging time. Both indentation modulus and hardness increase with the increase of high-temperature aging time. It was attributed to the promotion of diffusion bonding between Cu@Ag particles during short-term high-temperature aging, leading to enhanced microstructure densification and resistance to plastic deformation. In comparison to SCu@Ag, the FCu@Ag joints had higher indentation modulus and hardness overall. Specifically, the mean elastic modulus of FCu@Ag joints increased from 59.18 to 68.68 GPa after 300 h of high-temperature aging, with a growth rate of 16.1%. Simultaneously, the hardness also increased by 3.8%.

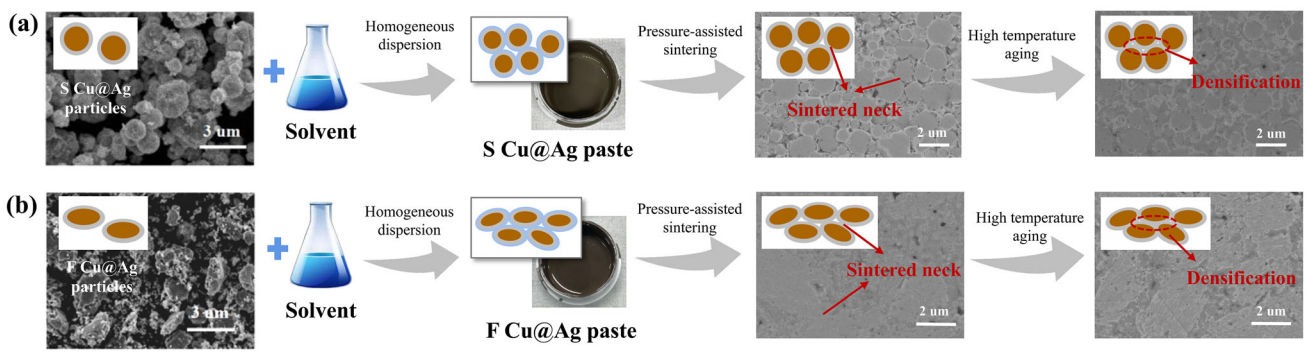

Fig. 13 The sintering evolution of Cu@Ag pastes

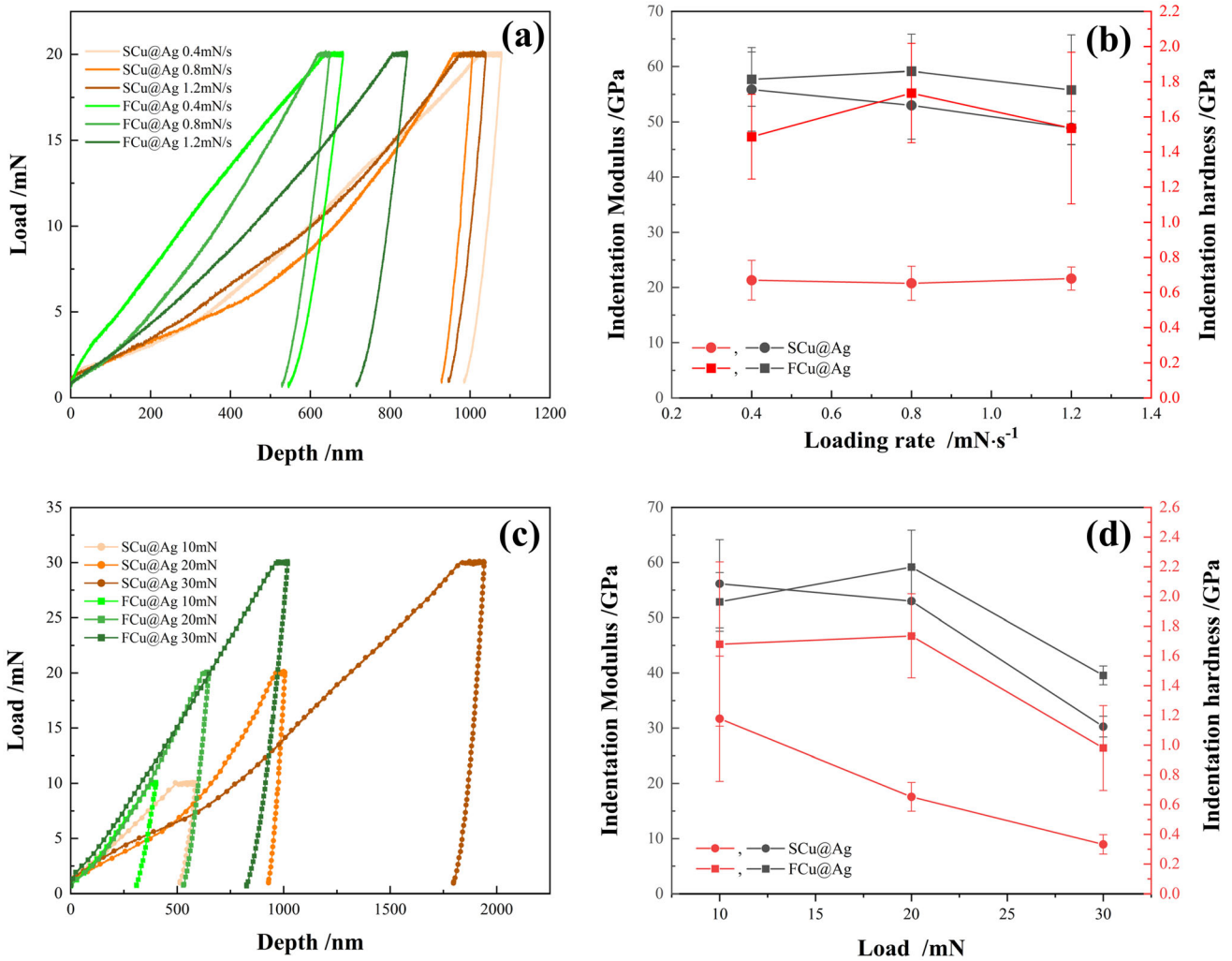

Fig. 14 **a**, **b** The effect of loading rate on the indentation properties of joints: **a** load–displacement curve; **b** indentation modulus and hardness; **c**, **d** the effect of applied load on the indentation properties of joints: **c** load–displacement curve, **d** indentation modulus and hardness

3.4.3 *Creep properties*

The investigation of the deformation behavior of sintered materials under high temperature and high stress using nanoindentation technology, as well as the analysis of their fatigue life and fracture behavior, holds great practical significance for their industrial application.Therefore, the creep characteristics of Cu@Ag joints were observed by holding them for 300 s under 20 mN, as shown in Fig. 16. The Cu@Ag sintered joints exhibited room temperature creep behavior, and the deeper creep displacement of SCu@Ag than FCu@Ag, which indicated that the SCu@Ag joints were more prone to creep. The creep displacement curves of Cu@Ag joints obtained in the nanoindentation test were divided into two stages, namely the initial creep stage and the steady creep stage. In the initial creep stage, the creep displacement increased rapidly with the increase of holding time, while the creep rate gradually decreased. This behavior was ascribed to the rapid nucleation of dislocation and rapid absorption by grain boundaries. Then it entered the steady creep stage, where the creep displacement slowly increased as the creep rate decreased and became stable. At the initial state of 0 h, the creep displacement of SCu@Ag and FCu@Ag were 150.19 nm and 55.32 nm, respectively. With high-temperature aging, the creep displacement of Cu@Ag joints decreased and the creep strain rate decreased. This indicated that the creep resistance increased after high-temperature aging. In contrast, FCu@Ag joints had smaller creep displacements than

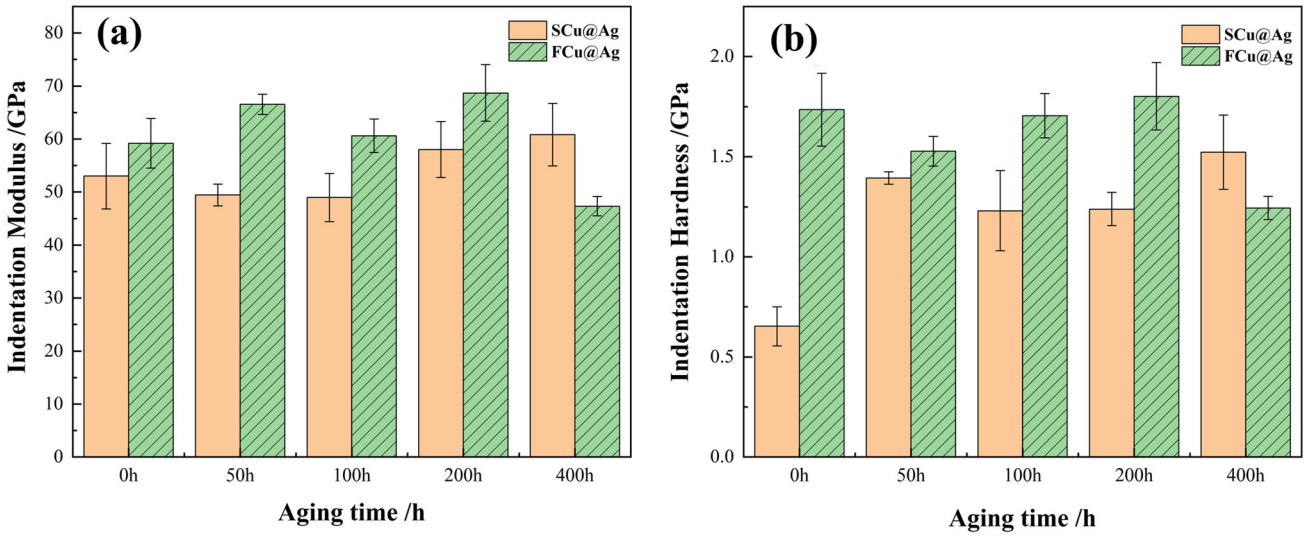

Fig. 15 Hardness and elasticity modulus of Cu@Ag samples after different high temperature aging time

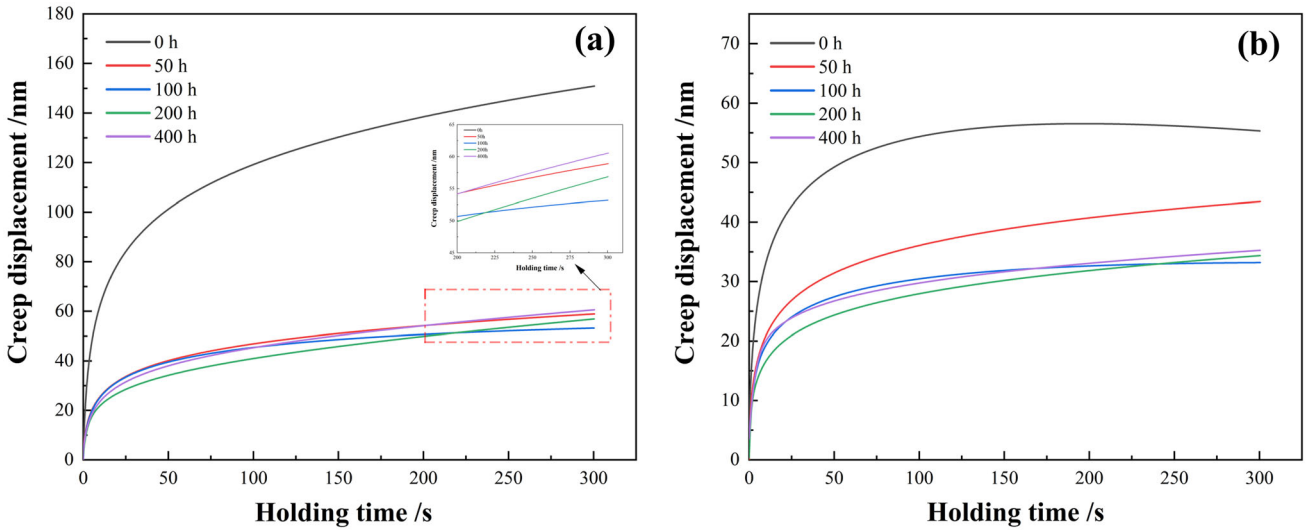

Fig. 16 Creep displacement of samples after different high-temperature aging time: **a** SCu@Ag, **b** FCu@Ag

SCu@Ag joints after the same high temperature aging time and exhibited better creep resistance.

To better evaluate the deformation mechanism of Cu@Ag joints, the double logarithmic curves of indentation strain rate and hardness were presented in Fig. 17. The strong linear correlation between the data indicated high fitting consistency. The hardness exhibited relatively little decrease during the load-holding process, suggesting that the creep deformation capacity of Cu@Ag joints at room temperature was limited. Regarding Cu@Ag joints, the strain rate sensitivity index m were mainly distributed between 0.01 and 0.05, which reflected that dislocation climbing was dominant in the steady creep stage. The slight fluctuations in data might have been caused by surface defects and the roughness of the samples. With the increase of high temperature aging time in the short term, the m value decreased, indicating that the creep resistance of Cu@Ag joints was enhanced. The reason behind this enhancement was the further promotion of microstructure densification and grain growth of Cu@Ag microparticles during the aging process. The grains gradually grew and the grain boundaries formed a continuous network, leading to enhanced interactions between dislocations and grain boundaries. The creep resistance of Cu@Ag particles was enhanced, thus limiting the room temperature creep behavior of the Cu@Ag joints. Consequently,

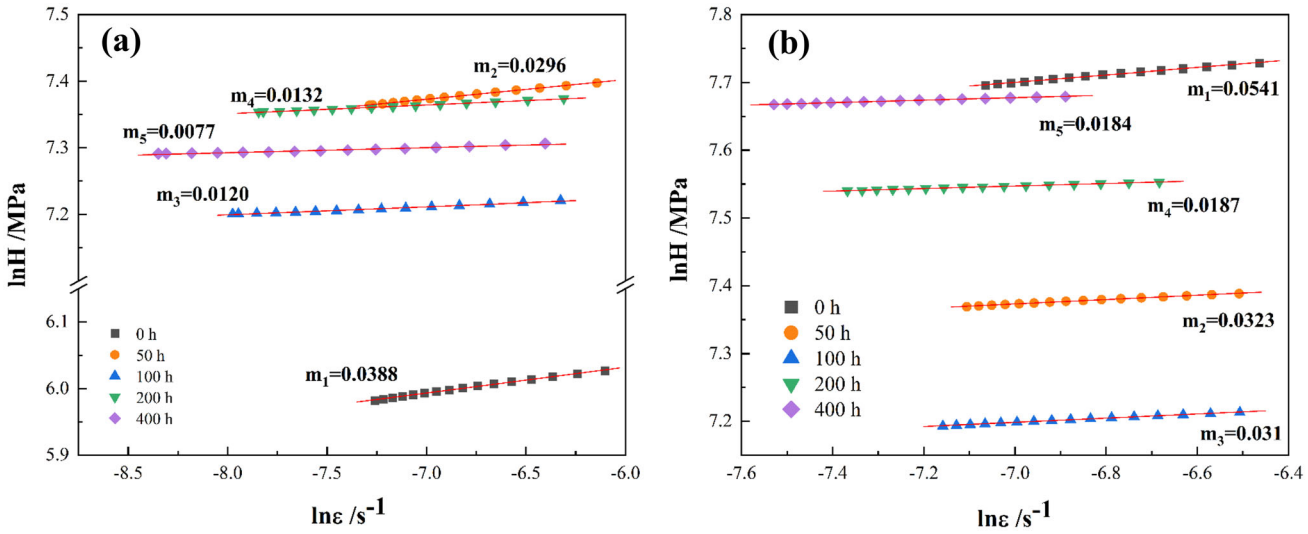

Fig. 17 Creep strain rate-hardness curves of Cu@Ag samples after different aging time

these results indicated that both spherical and flake-type Cu@Ag sintered joints exhibited excellent creep resistance and reliability.

3.4.4 *Constitutive model of sintered Cu@Ag particles*

The establishment of the constitutive model proved beneficial for understanding the elastic–plastic behavior of die attach materials, providing guidance for failure mechanism analysis and reliability assessment. Based on the inverse analysis algorithm, the constitutive relationship of Cu@Ag sintered joints with different particle morphologies was investigated by finite element modeling and compared with the results of nanoindentation experiments. The reverse analysis algorithm primarily relied on the nanoindentation loading stage curve for calculation and simulation. Firstly, an ideal elastoplastic model was assumed, and the stress intensification exponent was 0 ($n = 0$). The load–displacement curves were obtained through continuous iteration of FEM until the relative error with the nanoindentation result was less than 0.5%, as depicted in Fig. 18a. At this time, the characteristic stress σ_r of the SCu@Ag and FCu@Ag samples were 228.3 MPa and 357.57 MPa, respectively. Subsequently, the stress intensification index n obtained through dimensional theoretical analysis was substituted into the simulation for further iterative optimization, as shown in Fig. 18b. The congruity observed between the finite element method (FEM) results and experimental data in this figure substantiates the feasibility and precision of the elastic–plastic constitutive relationship for sintered Cu@Ag samples, as determined through inversion analysis. At this time, the characteristic strain values ε_r of SCu@Ag and FCu@Ag samples were 0.0248 and 0.0258, respectively. The yield stress σ_y was 24 MPa and 53.23 MPa, respectively. As a summary, Table 4 presented the constitutive parameters of SCu@Ag and FCu@Ag sintered samples. The Von Mises stress cloud diagrams of the Cu@Ag sintered samples under nanoindentation simulation were shown in Fig. 18c, d. The deformation of the Cu@Ag sintered samples was primarily concentrated in the contact area between the indenter and the samples, with stress propagating longitudinally and transversely in a circular manner. It was observed that FCu@Ag sintered particles exhibited a smaller stress concentration range compared to SCu@Ag sintered particles.

Finally, elastic–plastic constitutive models were developed for Cu@Ag sintered materials, providing descriptions of the stress–strain relationship for both SCu@Ag and FCu@Ag sintered particles, as represented by formulas (15) and (16) respectively. Figure 19 illustrated the corresponding micromorphology and stress–strain relationship curves of the sintered Cu@Ag particles. The yield stress (σ_y) of FCu@Ag sintered particles measured 53.23 MPa, which was 2.28 times higher than that of SCu@Ag sintered particles. This significant difference indicated that FCu@Ag sintered particles exhibited a notably higher yield stress and enhanced resistance to plastic deformation, resulting in reduced plastic deformation under the same conditions. In addition, the n value of FCu@Ag samples was also higher than that of SCu@Ag, which revealed that

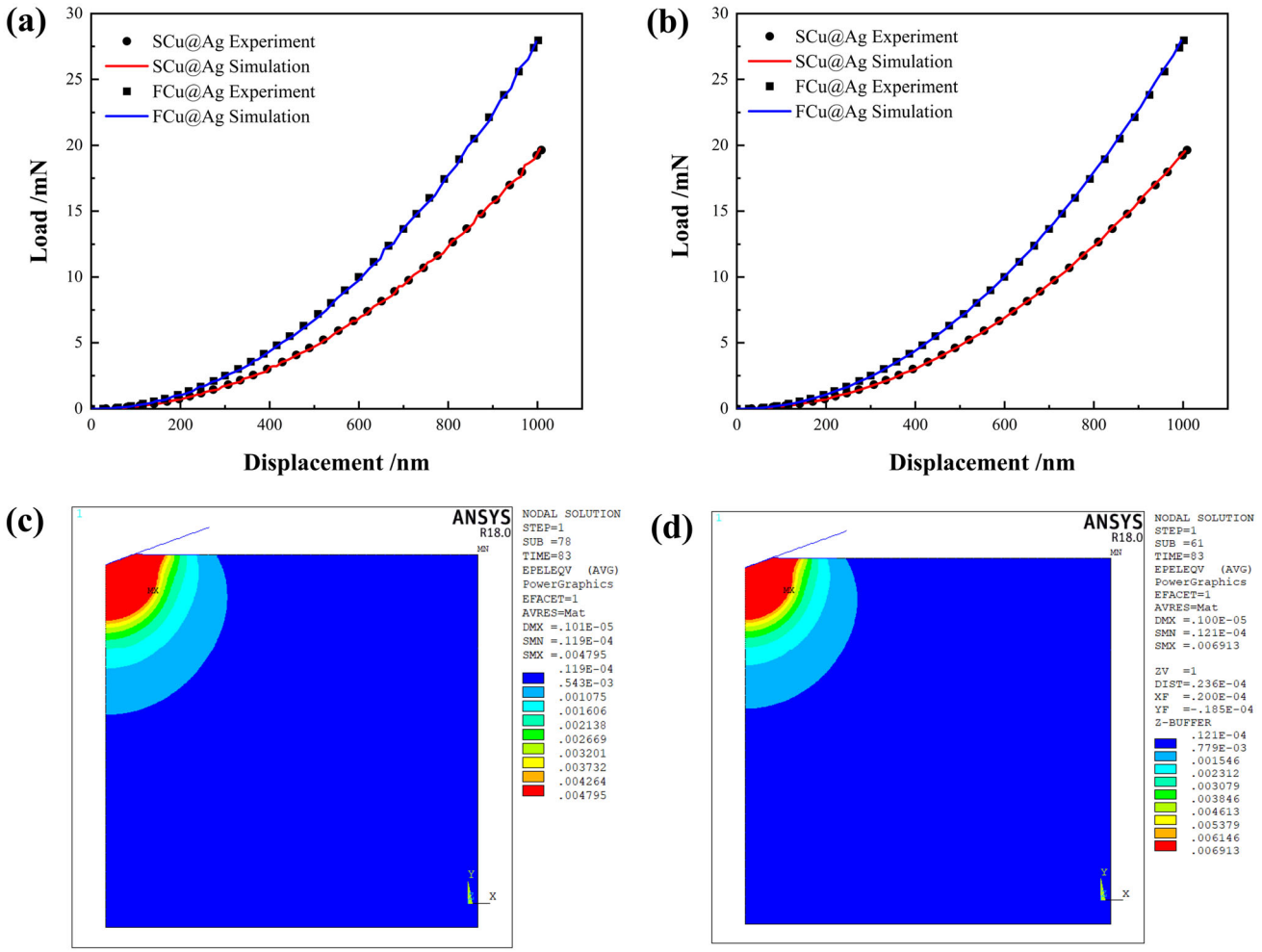

Fig. 18 Comparison of load–displacement curves predicted by the elastoplastic model of Cu@Ag sintered joints with experimental results: **a** $n = 0$, **b** $n \neq 0$; Results of Von Mises stress contours in finite element simulation: **c** SCu@Ag, **d** FCu@Ag

Table 4 Constitutive parameters of Cu@Ag sintered samples

	σ_r (MPa)	W_p/W_t	h_r/h_m	n	ε_r	σ_y (MPa)	R (GPa)	E (GPa)	H (GPa)
SCu@Ag	228.2979	0.8771	0.9093	0.5748	0.0248	24.0042	1.8951	47.75	0.83
FCu@Ag	357.5723	0.8118	0.8624	0.5838	0.0258	53.2296	3.003	51.87	1.28

FCu@Ag sintered particles had a higher strain hardening effect, leading to uniform deformation, which was beneficial to relieve stress concentration and suppressing cracks. In summary, FCu@Ag pastes demonstrated enhanced reliability and application value attributed to their superior deformation resistance and mechanical properties.

$$\sigma = \begin{cases} 47,750\epsilon & (\sigma \leq 24.00) \\ 24.00(1 + 1989.58\epsilon)^{0.5748} & (\sigma > 24.00) \end{cases}, \quad (15)$$

$$\sigma = \begin{cases} 51,870\epsilon & (\sigma \leq 53.23) \\ 53.23(1 + 974.45\epsilon)^{0.5838} & (\sigma > 53.23) \end{cases}. \quad (16)$$

4 Conclusions

In this study, sintering pastes based on two types of micro-size Cu@Ag particles with four solvent systems were successfully prepared and characterized

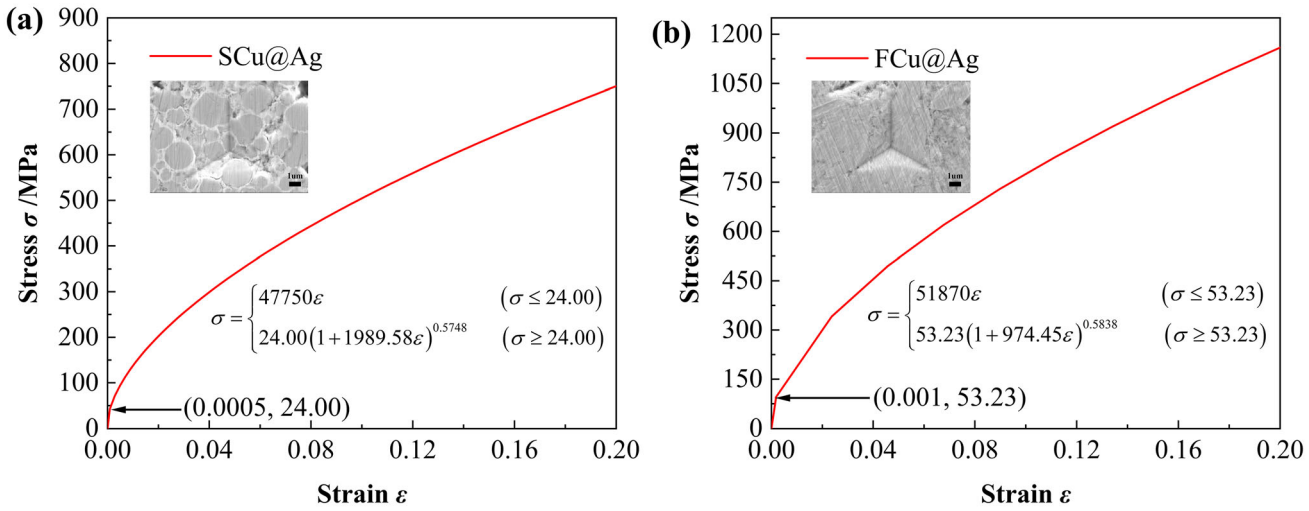

Fig. 19 Elastoplastic constitutive model of Cu@Ag samples: **a** SCu@Ag, **b** FCu@Ag

for die attachment. The main findings regarding this alternative material for silver sintering are as follows:

1. Both solvent systems and particle morphology played important roles in the properties of sintered joints. Particularly, the organic solvent system had a considerable impact on the sintering effect of FCu@Ag pastes. The positive effect of the Terpineol–polyethylene glycol solvent system on sintered Cu@Ag particles was not only to prevent particles agglomeration and oxidation due to the steric hindrance effect but also that the solvent can be almost completely volatilized during the sintering process, thereby facilitating further densification of the particles.
2. Flake-type Cu@Ag microparticles had a denser microstructure than spherical Cu@Ag due to their larger contact area. As a result, the shear strength of the FCu@Ag joints achieved 36.15 MPa, which was approximately 20% higher than that of SCu@Ag joints and deemed adequate for die-attach applications.
3. Among the sintering process parameters, the mechanical properties of Cu@Ag joints were most significantly influenced by the sintering temperature, while the sintering pressure had the least effect. Furthermore, the optimized process parameters (250 °C, 20 MPa, 10 min) were proposed as a reference for industrial applications. Notably, FCu@Ag joints demonstrated satisfying high-temperature reliability and thermal cycling resistance, maintaining a bonding strength of over 70 MPa even after 400 h of high-temperature aging.
4. The micromechanical properties of Cu@Ag joints after aging were evaluated by nanoindentation, encompassing hardness, elastic modulus and creep properties. The results revealed that the micromechanical properties of FCu@Ag joints were not significantly affected by 400 h of high-temperature aging. Moreover, the construction of elastic–plastic constitutive models for Cu@Ag sinter materials offered valuable guidance for analyzing its mechanical behavior and reliability life in-depth.

In conclusion, the FCu@Ag paste proposed in this paper not only had considerable mechanical strength, but also had satisfying creep resistance and high-temperature reliability, which provided a promising solution for power electronic packaging.

Acknowledgements

In this work, the authors would like to thank to Heraeus Materials Technology Shanghai Ltd. for characterization support.

Author contributions

HC conducted the experiment, analyzed the data and wrote the manuscript. XW performed the experiment and analyzed some experimental data. ZZ designed the experiment and collected the data. GZ and JZ provided the experimental equipment and analytical techniques. PL supervised the research.

Funding

Funding was provided by Heraeus Materials Technology Shanghai Ltd.

Data availability

The data that support the finding of this study are available from the corresponding author upon reasonable request.

Declarations

Competing interests The authors declare that they have no conflict of interest.

Ethical approval This study does not include any experiments involving humans or animals. Ethical approval does not apply to this article.

References

1. A. Roshanghias, P. Malago, J. Kaczynski et al., Energies (2021). https://doi.org/10.3390/en14082176
2. V.R. Manikam, C. Kuan Yew, IEEE Trans. Compon. Packag. Manuf. Technol. (2011). https://doi.org/10.1109/tcpmt.2010.2100432
3. S. Zhang, X. Xu, T. Lin, P. He, J. Mater. Sci. (2019). https://doi.org/10.1007/s10854-019-01790-3
4. N. Jiang, L. Zhang, Z.Q. Liu et al., Sci. Technol. Adv. Mater. (2019). https://doi.org/10.1080/14686996.2019.1640072
5. M. Xiong, L. Zhang, J. Mater. Sci. (2018). https://doi.org/10.1007/s10853-018-2907-y
6. Z. Zhang, C. Chen, Y. Yang et al., J. Alloys Compd. (2019). https://doi.org/10.1016/j.jallcom.2018.11.251
7. S.K. Bhogaraju, O. Mokhtari, F. Conti, G. Elger, Scr. Mater. (2020). https://doi.org/10.1016/j.scriptamat.2020.02.045
8. P. Zhao, X. Li, Y. Mei, G.-Q. Lu, Mater. Lett. (2022). https://doi.org/10.1016/j.matlet.2021.131603
9. K.S. Siow, J. Electron. Mater. (2014). https://doi.org/10.1007/s11664-013-2967-3
10. J. Liu, H. Chen, H. Ji, M. Li, ACS Appl. Mater. Interfaces (2016). https://doi.org/10.1021/acsami.6b10280
11. Y. Peng, Y. Mou, J. Liu, M. Chen, J. Mater. Sci. (2020). https://doi.org/10.1007/s10854-020-03380-0
12. H. Fang, C. Wang, S. Zhou et al., J. Mater. Sci. (2020). https://doi.org/10.1007/s10854-020-03207-y
13. L.D. Carro, A.A. Zinn, P. Ruch, F. Bouville, A.R. Studart, T. Brunschwiler, J. Electron. Mater. (2019). https://doi.org/10.1007/s11664-019-07452-8
14. Y. Mou, J. Liu, H. Cheng, Y. Peng, M. Chen, JOM (2019). https://doi.org/10.1007/s11837-019-03517-5
15. C.H. Lee, E.B. Choi, J.-H. Lee, Scr. Mater. (2018). https://doi.org/10.1016/j.scriptamat.2018.02.029
16. E.B. Choi, J.-H. Lee, Appl. Surf. Sci. (2021). https://doi.org/10.1016/j.apsusc.2021.149156
17. Y. Tian, Z. Jiang, C. Wang et al., RSC Adv. (2016). https://doi.org/10.1039/c6ra16474a
18. T. Michaud, T. Baffie, S.S. Nobre, J.-M. Missiaen, D. Bouvard, J.-P. Simonato, Materialia (2020). https://doi.org/10.1016/j.mtla.2020.100871
19. C.-H. Hsiao, W.-T. Kung, J.-M. Song, J.-Y. Chang, T.-C. Chang, Mater. Sci. Eng. (2017). https://doi.org/10.1016/j.msea.2016.12.084
20. Y. Bao, A. Wu, H. Shao, Y. Zhao, L. Liu, G. Zou, J. Mater. Sci. (2018). https://doi.org/10.1007/s10853-018-2809-z
21. H. Zhang, W. Wang, H. Bai et al., J. Alloys Compd. (2019). https://doi.org/10.1016/j.jallcom.2018.10.067
22. X. Long, Y. Guo, Y. Su, K.S. Siow, C. Chen, J. Mater. Sci. (2022). https://doi.org/10.1007/s10854-021-07474-1
23. X. Long, Q.P. Jia, Z. Li, S.X. Wen, Int. J. Solids Struct. (2020). https://doi.org/10.1016/j.ijsolstr.2020.01.014
24. G. He, W. Hongcheng, Y. Yao, J. Mater. Sci. (2021). https://doi.org/10.1007/s10853-021-06426-8
25. X. Long, Q. Jia, Z. Shen, M. Liu, C. Guan, Mech. Mater. (2021). https://doi.org/10.1016/j.mechmat.2021.103881
26. H. Zhang, Y. Liu, L. Wang, F. Sun, X. Fan, G. Zhang, Results Phys. (2019). https://doi.org/10.1016/j.rinp.2018.12.026
27. J. Fan, D. Jiang, H. Zhang et al., Results Phys. (2022). https://doi.org/10.1016/j.rinp.2021.105168
28. W.C. Oliver, G.M. Pharr, J. Mater. Res. Technol. (1992). https://doi.org/10.1557/jmr.1992.1564
29. K. Tunvisut, N.P. O'Dowd, E.P. Busso, Int. J. Solids Struct. (2001). https://doi.org/10.1016/S0020-7683(00)00017-2
30. J. Luo, J. Lin, Int. J. Solids Struct. (2007). https://doi.org/10.1016/j.ijsolstr.2007.01.029